



INTEGRAL Discovery of a Burst with Associated Radio Emission from the Magnetar SGR 1935+2154

S. Mereghetti¹, V. Savchenko², C. Ferrigno², D. Götz³, M. Rigoselli¹, A. Tiengo⁴, A. Bazzano⁵, E. Bozzo², A. Coleiro⁶, T. J.-L. Courvoisier², M. Doyle⁷, A. Goldwurm⁶, L. Hanlon⁷, E. Jourdain^{8,9}, A. von Kienlin¹⁰, A. Lutovinov¹¹, A. Martin-Carrillo⁷, S. Molkov¹¹, L. Natalucci⁵, F. Onori⁵, F. Panessa⁵, J. Rodi⁵, J. Rodriguez³, C. Sánchez-Fernández¹², R. Sunyaev^{11,13}, and P. Ubertini⁵

¹ INAF—Istituto di Astrofisica Spaziale e Fisica Cosmica, Via A. Corti 12, I-20133 Milano, Italy; sandro.mereghetti@inaf.it

² ISDC, Department of Astronomy, University of Geneva, Chemin d'Écogia, 16 CH-1290 Versoix, Switzerland

³ AIM-CEA/DRF/Irfu/Département d'Astrophysique, CNRS, Université Paris-Saclay, Université de Paris, Orme des Merisiers, F-91191 Gif-sur-Yvette, France

⁴ Scuola Universitaria Superiore IUSS, Piazza della Vittoria 15, I-27100 Pavia, Italy

⁵ INAF—Institute for Space Astrophysics and Planetology, Via Fosso del Cavaliere 100, I-00133 Rome, Italy

⁶ APC, AstroParticule et Cosmologie, Université Paris Diderot, CNRS/IN2P3, CEA/Irfu, Observatoire de Paris Sorbonne Paris Cité, 10 rue Alice Domont et Léonie Duquet, F-75205 Paris Cedex 13, France

⁷ Space Science Group, School of Physics, University College Dublin, Belfield, Dublin 4, Ireland

⁸ CNRS, IRAP, 9 Av. colonel Roche, BP 44346, F-31028 Toulouse cedex 4, France

⁹ Université de Toulouse, UPS-OMP, IRAP, Toulouse, France

¹⁰ Max-Planck-Institut für Extraterrestrische Physik, Garching, Germany

¹¹ Space Research Institute of Russian Academy of Sciences, Profsoyuznaya 84/32, 117997 Moscow, Russia

¹² European Space Astronomy Centre (ESA/ESAC), Science Operations Department, E-28691 Villanueva de la Cañada, Madrid, Spain

¹³ Max Planck Institute for Astrophysics, Karl-Schwarzschild-Str. 1, D-85741 Garching b. Munchen, Germany

Received 2020 May 12; revised 2020 July 2; accepted 2020 July 3; published 2020 July 27

Abstract

We report on International Gamma-Ray Astrophysics Laboratory (INTEGRAL) observations of the soft γ -ray repeater SGR 1935+2154 performed between 2020 April 28 and May 3. Several short bursts with fluence of $\sim 10^{-7}$ – 10^{-6} erg cm⁻² were detected by the Imager on-board INTEGRAL (IBIS) instrument in the 20–200 keV range. The burst with the hardest spectrum, discovered and localized in real time by the INTEGRAL Burst Alert System, was spatially and temporally coincident with a short and very bright radio burst detected by the Canadian Hydrogen Intensity Mapping Experiment (CHIME) and Survey for Transient Astronomical Radio Emission 2 (STARE2) radio telescopes at 400–800 MHz and 1.4 GHz, respectively. Its lightcurve shows three narrow peaks separated by ~ 29 ms time intervals, superimposed on a broad pulse lasting ~ 0.6 s. The brightest peak had a delay of 6.5 ± 1.0 ms with respect to the 1.4 GHz radio pulse (that coincides with the second and brightest component seen at lower frequencies). The burst spectrum, an exponentially cutoff power law with photon index $\Gamma = 0.7_{-0.2}^{+0.4}$ and peak energy $E_p = 65 \pm 5$ keV, is harder than those of the bursts usually observed from this and other magnetars. By the analysis of an expanding dust-scattering ring seen in X-rays with the Neil Gehrels Swift Observatory X-ray Telescope (XRT) instrument, we derived a distance of $4.4_{-1.3}^{+2.8}$ kpc for SGR 1935+2154, independent of its possible association with the supernova remnant G57.2+0.8. At this distance, the burst 20–200 keV fluence of $(6.1 \pm 0.3) \times 10^{-7}$ erg cm⁻² corresponds to an isotropic emitted energy of $\sim 1.4 \times 10^{39}$ erg. This is the first burst with a radio counterpart observed from a soft γ -ray repeater and it strongly supports models based on magnetars that have been proposed for extragalactic fast radio bursts.

Unified Astronomy Thesaurus concepts: Magnetars (992); Soft gamma-ray repeaters (1471); Interstellar scattering (854); Radio bursts (1339)

1. Introduction

Magnetars are neutron stars powered mainly by magnetic energy dissipation that are characterized by strong variability on several timescales (see Mereghetti et al. 2015; Turolla et al. 2015; Kaspi & Beloborodov 2017 for reviews). Many known magnetars were first discovered as soft gamma-ray repeaters (SGRs), i.e., sources of multiple bursts of hard X-rays, typically shorter than 1 s and with peak luminosity up to $\sim 10^{39-41}$ erg s⁻¹. Longer and more energetic bursts have also been observed from a few SGRs, with the most extreme cases, known as giant flares, reaching peak luminosity as large as 10^{47} erg s⁻¹ and releasing a total energy up to 10^{46} erg (e.g., Palmer et al. 2005). All the currently known magnetars are in the Galaxy or in the Magellanic Clouds (Olausen & Kaspi 2014).

Fast radio bursts (FRBs; see Cordes & Chatterjee 2019; Petroff et al. 2019 for reviews) are an enigmatic class of sources emitting short (~ 1 – 10 ms) pulses of radio emission with peak fluxes of ~ 0.1 – 100 Jy at 1.4 GHz and dispersion measures (DMs) in excess of the Milky Way values along their lines of sight. Their extragalactic nature has been demonstrated by the association of a few FRBs with host galaxies in the redshift range 0.0337–0.4755 (Prochaska et al. 2019; Marcote et al. 2020), and possibly up to $z = 0.66$ (Ravi et al. 2019). A large variety of models have been proposed for FRBs (see Platts et al. 2019 for an extensive and updated list), but no consensus has been reached yet on the nature of these sources. Although many of these models involve magnetars, there has been no confirmed association between an FRB and a high-energy bursting source until now.

Here we report on hard X-ray observations of the magnetar SGR 1935+2154 carried out with the International Gamma-Ray Astrophysics Laboratory (INTEGRAL) satellite in 2020 April–May. In particular, we present the properties of a short and hard burst for which a spatially and temporally coincident FRB has been detected in the 400–800 MHz band (The CHIME/FRB Collaboration et al. 2020b) and at 1.4 GHz (Bochenek et al. 2020). This is the first detection of a pulse of radio emission clearly associated with an SGR burst, thus providing an intriguing connection between magnetars and FRBs. We also report a new estimate of the distance of SGR 1935+2154 based on the analysis of a dust-scattering ring detected in soft X-rays with the Neil Gehrels Swift Observatory (Kennea et al. 2020).

2. SGR 1935+2154

SGR 1935+2154 was discovered through the detection of hard X-ray bursts with the Swift/Burst Alert Telescope (BAT) instrument in 2014 July (Stamatikos et al. 2014). Its magnetar nature was confirmed by follow-up X-ray observations that revealed a spin period $P = 3.25$ s and period derivative $\dot{P} = 1.43 \times 10^{-11}$ s s $^{-1}$ (Israel et al. 2016), corresponding to a characteristic age of 3.6 kyr and a dipole magnetic field of 2.2×10^{14} G. A very faint ($H \sim 24$) near-infrared counterpart was identified, thanks to its variability, by the Hubble Space Telescope (Levan et al. 2018). Pulsed radio emission has been observed in a few transient magnetars, but not in SGR 1935+2154 (Burgay et al. 2014; Surnis et al. 2014; Israel et al. 2016; Pearlman et al. 2020), with the most constraining upper limits of 14 μ Jy (4.6 GHz) and 7 μ Jy (1.4 GHz) derived by Younes et al. (2017). Single pulses were also undetected down to limits of ~ 70 mJy (Israel et al. 2016) and ~ 10 –20 mJy (Younes et al. 2017).

Like most known magnetars, SGR 1935+2154 lies in the Galactic plane ($l = 57.25$ deg, $b = +0.82$ deg), at an unknown distance. The magnetar could be associated with the supernova remnant G57.2+0.8, for which distances of ~ 12.5 kpc (Kothes et al. 2018), 4.5–9 kpc (Ranasinghe et al. 2018), and 6.6 ± 0.7 (Zhou et al. 2020) have been derived. In the following, we will scale all the quantities to the distance $d = 4.4d_{4.4}$ kpc, derived from our analysis of the dust-scattering ring (see Section 4).

Since its discovery, SGR 1935+2154 has been rather active, emitting short bursts in 2015 February and 2016 May–July (Younes et al. 2017; Lin et al. 2020a), as well as an intermediate flare on 2015 April 12 (Kozlova et al. 2016). Recently, SGR 1935+2154 has entered a new period of activity (Hurley et al. 2020; Veres et al. 2020) that culminated with the emission of a “burst forest,” i.e., tens of bursts in a short time interval, on 2020 April 27–28 (Fletcher & Fermi GBM Team 2020; Palmer 2020; Younes et al. 2020).

3. INTEGRAL Data Analysis and Results

Our results are based mainly on data obtained with the Imager on-board INTEGRAL (IBIS) instrument (Ubertini et al. 2003) that provides images in a 30×30 deg 2 field of view thanks to a coded mask coupled to two detector arrays: INTEGRAL Soft Gamma Ray Imager (ISGRI) and Pixellated Imaging Caesium Iodide Telescope (PICsIT). ISGRI collects photon-by-photon events, tagged with a resolution of 61 μ s, in the nominal 15–1000 keV energy range (Lebrun et al. 2003). Higher energies are covered by PICsIT (Labanti et al. 2003),

Table 1

Log of INTEGRAL Observations of SGR 1935+2154 in 2020 April–May

Start Time MM DD HH:MM (UTC)	End Time	ON-time ^a (ks)	Off-axis Angle (deg)
Apr 22 18:54	Apr 23 07:44	41.1(89%)	6.2–17.0
Apr 25 10:46	Apr 26 01:29	42.8(80%)	4.2–18.6
Apr 28 02:37	Apr 29 12:54	102.6(83%)	0.5–18.2
Apr 30 18:27	Apr 30 23:08	8.6(51%)	12.9–16.0
May 1 02:08	May 1 04:27	7.9(94%)	15.4–19.0
May 1 11:51	May 1 14:10	7.9(95%)	13.1–16.0
May 1 17:10	May 1 19:29	7.9(94%)	15.4–19.0
May 3 10:53	May 5 05:30	127.3(82%)	0.6–18.4

Note.

^a The source ON-time takes into account the bad time intervals, due to, e.g., telemetry gaps. In parentheses, the fraction of time with SGR 1935+2154 in the IBIS/ISGRI field of view.

which, besides other data types, produces spectral-timing data with a 7.8 ms integration time allowing the detection of impulsive events in the 200–2600 keV energy range.

The position of SGR 1935+2154 was repeatedly in the field of view of IBIS, for a total on-time of ~ 350 ks between 18:54 of 2020 April 22 and 05:30 UTC of 2020 May 5 (see Table 1). All the IBIS/ISGRI data are analyzed in real time at the INTEGRAL Science Data Center (ISDC; Courvoisier et al. 2003) by the INTEGRAL Burst Alert System (IBAS), a software for the automatic search and rapid localization of gamma-ray bursts and other transient sources (Mereghetti et al. 2003).

On 2020 April 28, IBAS triggered on two bursts, at 09:51:05 UTC and 14:34:24 UTC. It derived their positions with accuracies of $3/7$ and $2/8$, respectively, and distributed the public Alert Packets reporting the identification of SGR 1935+2154 as the origin of these triggers after less than 10 s. An analysis of the ISGRI data carried out off-line with the standard imaging analysis software (Goldwurm et al. 2003) confirmed the association of both events with SGR 1935+2154. For example, the second burst is detected at coordinates R.A. = $19^{\text{h}}34^{\text{m}}53^{\text{s}}.8$, $+21^{\circ}53'46''$ (with 90% c.l. error radius of $1/4$), that differ by $0/5$ from those of SGR 1935+2154.

These two bursts were also detected by the INTEGRAL Spectrometer Instrument¹⁴ (SPI; Vedrenne et al. 2003) and by its Anti-Coincidence Shield (ACS; von Kienlin et al. 2003). The latter provides lightcurves with 50 ms resolution at energies above ~ 80 keV, with maximum sensitivity for directions perpendicular to the satellite pointing (Savchenko et al. 2017).

3.1. The Radio-loud Burst

The brightest of the two bursts discovered by IBAS (burst-G of Table 2) is temporally coincident with the radio burst discovered by the Canadian Hydrogen Intensity Mapping Experiment (CHIME) and Survey for Transient Astronomical Radio Emission 2 (STARE2) radio telescopes (Bochenek et al. 2020; The CHIME/FRB Collaboration et al. 2020b). Burst-G was also detected by X-ray instruments on the Insight-Hard X-Ray Modulation Telescope (HXMT), Konus-Wind, and

¹⁴ The signal-to-noise ratio of the bursts in SPI is much lower than that in ISGRI, and the data are affected by telemetry saturation features. Therefore, we do not use the SPI data in the present paper.

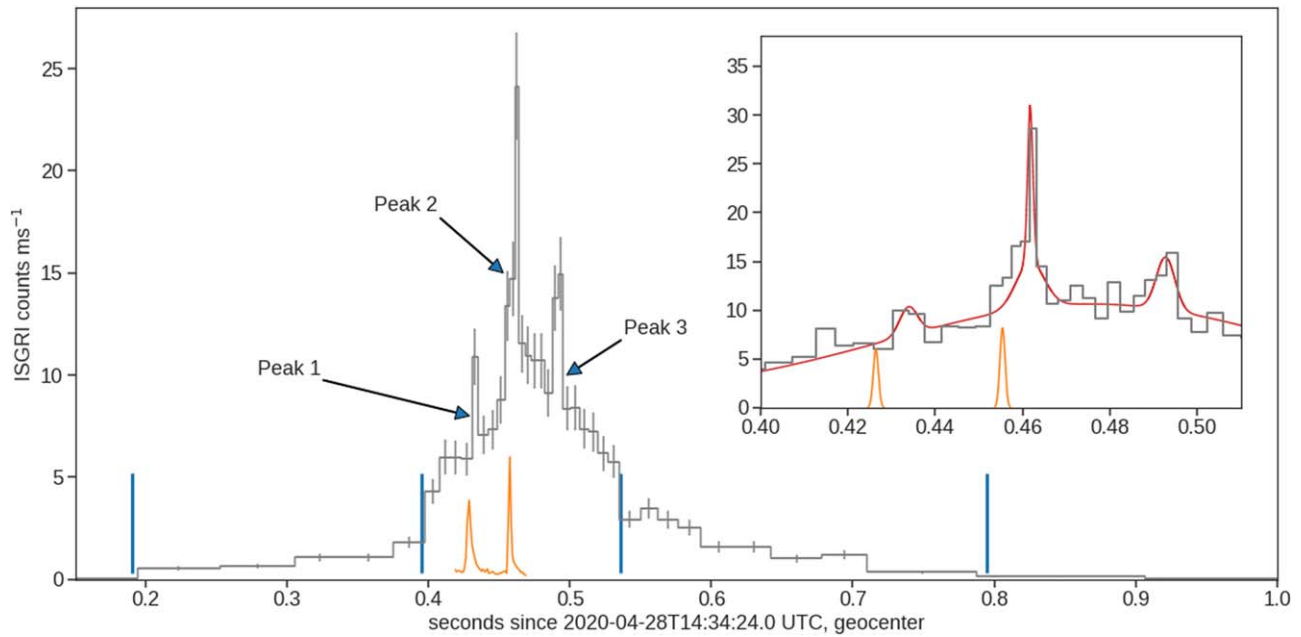


Figure 1. Background-subtracted and dead-time-corrected lightcurve of burst-G in the 20–200 keV range obtained with the IBIS/ISGRI instrument. We used an adaptive binning to ensure at least 40 counts per time bin. All the times are in the geocentric frame and referred to $t_0 = 14:34:24$ UTC of 2020 April 28. The blue lines (at 0.19, 0.395, 0.536, and 0.79 s) indicate the time intervals used for the spectral and imaging analysis. The orange line (adapted from Figure 1 of The CHIME/FRB Collaboration et al. 2020b) marks the position of the radio pulses. The inset shows the brightest part of the burst, binned with a minimum of 25 counts per bin. The red line is the fit to the ISGRI unbinned data with a combination of Gaussian curves (see the text for details), that yields the following times for the three narrow peaks: $t_1 = 0.434^{+0.004}_{-0.002}$ s, $t_2 = 0.462 \pm 0.001$ s, and $t_3 = 0.493^{+0.002}_{-0.003}$ s. The radio pulses are represented in the inset with two Gaussian curves centered at 0.42648 and 0.45545 s.

Table 2
Bursts Observed in the Selected Observation Period (see Table 1)

Name	Trigger Time YYYY MM DD HH:MM:SS.S	Duration (s)	S/N ^a	Total Counts ^b	Fluence (10^{-7} erg cm $^{-2}$)	Γ	Off-axis Angle (deg)
A	2020 Apr 28 03:47:52.200	0.06	17	33 (2.1)	$1.3^{+0.2}_{-0.3}$...	15.2
B	2020 Apr 28 04:09:47.300	0.09	14	35 (2.7)	$1.0^{+0.2}_{-0.3}$...	15.2
C	2020 Apr 28 05:56:30.637	0.11	14	113 (10.2)	$1.4^{+0.2}_{-0.1}$	$3.0^{+0.5}_{-0.4}$	12.4
D	2020 Apr 28 06:07:47.037	0.17	12	110 (18.1)	$1.0^{+0.2}_{-0.1}$	$3.2^{+0.6}_{-0.3}$	12.4
E	2020 Apr 28 08:03:34.370	0.04	9	18 (1.8)	<0.7	...	14.2
F	2020 Apr 28 09:51:04.894	0.38	10	201 (56.0)	$1.0^{+0.4}_{-0.1}$	$3.8^{+1.2}_{-0.4}$	10.4
G ^c	2020 Apr 28 14:34:24.357	0.75	23	1629 (159.1)	$6.9^{+0.3}_{-0.2}$	$2.1^{+0.1}_{-0.1}$	8.1
H	2020 Apr 29 09:10:53.895	0.06	8	7 (0.7)	<0.8	...	15.6
I	2020 May 3 23:25:13.469	0.15	46	136 (3.1)	$10.5^{+1.4}_{-1.2}$	$3.3^{+0.5}_{-0.3}$	16.9

Notes.

^a Signal-to-noise ratio extracted from the lightcurve binned at 100 ms used to detect the bursts.

^b Total raw counts collected by IBIS in the indicated time range; in parentheses, the number of counts expected from the background.

^c This is the burst with associated radio emission. The spectral parameters given here are those of the power-law fit, to facilitate the comparison with the other bursts. See the text for the more appropriate values obtained with other spectral models.

Astrorivelatore Gamma ad Immagini LEggero (AGILE) satellites (Li et al. 2020; Ridnaia et al. 2020b; Tavani et al. 2020a).

The background-subtracted and dead-time-corrected lightcurve of burst-G, as measured with IBIS/ISGRI in the 20–200 keV energy range, is plotted in Figure 1, where all the times are in the geocentric frame.¹⁵ We used only detector pixels illuminated by more than 40% by the source and an adaptive binning to get a minimum of 40 counts per time bin.

We also show in Figure 1 the position of the CHIME radio pulses. The X-ray lightcurve shows a main pulse lasting about 0.2 s with three narrow peaks. To estimate the arrival times of the peaks we fitted the ISGRI unbinned data with a combination of Gaussian curves, taking into account dead-time effects while computing the probability of events arrival from the model rate. The main pulse is well described by two broad Gaussians, and the three peaks by narrow ones centered at $t_1 = 0.434^{+0.004}_{-0.002}$ s, $t_2 = 0.462 \pm 0.001$ s, and $t_3 = 0.493^{+0.002}_{-0.003}$ s (we give all the times of burst-G relative to $t_0 = 14:34:24$ UTC). The second peak shows a narrow core with two wings; hence, we modeled it with the combination of two Gaussians with the same center.

¹⁵ INTEGRAL was at 128 Mm from Earth, resulting in a delay of 0.195 s for the burst to reach the Earth center. All the times quoted in this paper are corrected for the light travel time from the satellite to the Earth center.

The main pulse ([0.395–0.536 s]) is preceded and followed by fainter, slowly varying emission. Thanks to the ISGRI imaging capabilities, we can verify that such emission is due to the source and not to background fluctuations. In fact, SGR 1935+2154 is clearly detected in the images extracted from the time intervals [0.19–0.395 s] and [0.536–0.79 s], with statistical significance of 5.3 and 8.8σ , respectively. These intervals are highlighted by vertical blue lines in Figure 1.

We carried out a spectral analysis using the Xspec software v. 12.11.0 and give uncertainties at 68% confidence level. To estimate the uncertainties of the best-fit parameters we applied the Monte Carlo Markov Chain method with the Goodman–Weare algorithm (Goodman & Weare 2010) and derived the 1σ confidence intervals from the 16th and 84th percentiles of posteriors. We used uninformative uniform priors for the slope of the power law in all models and uninformative uniform logarithmic priors (known as Jeffreys priors) for all other parameters. We ignore channels below 32 keV, owing to systematic uncertainty in the response calibration and limit our fits below 300 keV, where the source is significantly detected. Besides all the effects taken into account by the standard INTEGRAL analysis software, the fluxes given below are corrected for the effect of dead time, which is of 0.1 ms in each of the eight detector modules that compose the ISGRI instrument.

We extracted a total spectrum from a time interval of 0.6 s starting at $t_p + 0.19$ s, as well as three spectra for the subintervals¹⁶ indicated by the blue lines in Figure 1. A single power law could not fit well the total spectrum (photon index $\Gamma = 2.1 \pm 0.1$, reduced $\chi^2_\nu = 3.6$ for 14 degrees of freedom (dof)). Using an exponentially cutoff power law, we obtained a best-fit photon index $\Gamma = 0.7^{+0.4}_{-0.2}$, peak energy $E_p = 65 \pm 5$ keV, and 20–200 keV flux of $(10.2 \pm 0.5) \times 10^{-7}$ erg s⁻¹ cm⁻² ($\chi^2_\nu = 1.8$ for 13 dof).

The X-ray spectra of SGR bursts are often fit also with the sum of two blackbody models. In this case, to avoid the two components swapping in the posterior sampling, we imposed that one temperature is below 20 keV and the other one above this value in our prior limits. We found a best fit with temperatures $kT_1 = 11.0 \pm 1.3$ keV, $kT_2 = 30 \pm 4$ keV and radii $R_1 = (0.83^{+0.18}_{-0.14}) d_{4.4}$ km, $R_2 = (0.12 \pm 0.04) d_{4.4}$ km ($\chi^2_\nu = 1.6$ for 12 dof).

To search for possible spectral variations, we first fitted simultaneously the spectra of the three subintervals with the cutoff power-law model, keeping both Γ and E_p tied among the three spectra, and then checked with the F-test statistics the significance of fit improvements obtained with either or both parameters free to vary. Imposing only a common slope, we obtained $\chi^2/\text{dof} = 46/41$ (compared to $\chi^2/\text{dof} = 58/43$ with both parameters tied), which corresponds to 0.7% chance probability of the fit improvement. The best-fit parameters are $\Gamma = 0.62^{+0.22}_{-0.18}$, E_p of 34 ± 8 keV (before main pulse), 60 ± 5 keV (main pulse), and 125^{+50}_{-29} keV (after main pulse), and 20–200 keV fluxes of $1.9^{+0.2}_{-0.3}$, 32^{+2}_{-1} , and $4.6^{+0.4}_{-0.6}$ in units of 10^{-7} erg s⁻¹ cm⁻², respectively. This result gives some evidence for a spectral hardening as a function of time (see Figure 2). Keeping instead a common E_p and letting the slopes

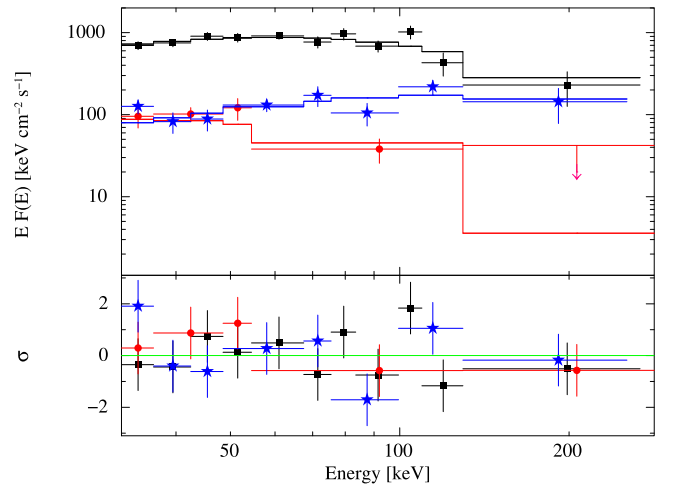


Figure 2. Unfolded energy spectra of burst-G fitted with a cutoff power-law model (top panel). The three spectra refer to the main pulse (black squares) and to the intervals before (red circles) and after (blue stars) the main pulse. The spectra have been rebinned for plotting purposes. The lower panel shows the residuals in units of σ .

as free parameters gave a worse fit ($\chi^2/\text{dof} = 52/41$), indicating that the spectral evolution is driven by an increase of the peak energy, rather than a change in slope. By leaving all parameters free, we found no statistically significant improvement with respect to using a common slope.

We extracted also the spectra of the three narrow peaks, but their small number of counts does not allow a meaningful spectral analysis. Adopting the best-fit cutoff power-law parameters of the total spectrum, we obtained the following 20–200 keV fluxes in units of 10^{-7} erg cm⁻² s⁻¹: 36^{+7}_{-7} (Peak-1, [0.431–0.435 s]), 58^{+5}_{-8} (Peak-2, [0.454–0.464 s]), and 54^{+6}_{-8} (Peak-3, [0.487–0.495 s]).

Analysis of the PICsIT spectral-timing data corresponding to the total time interval yielded a 3σ upper limit of 1.6×10^{-7} erg cm⁻² s⁻¹ in the 200–500 keV energy range, assuming the cutoff power-law spectral parameters from ISGRI.

The SPI/ACS data are routinely analyzed to search for bursts on different timescales. Burst-G reached the highest signal-to-noise ratio (4.65) in the data binned at 0.65 s. We note that, based only on time coincidence (following Connaughton et al. 2016) and independently of the IBIS/ISGRI detection, the ACS data give an association with the radio burst with a false-alarm probability at the level of 2.9σ .

3.2. Other Bursts

A more sensitive search for other bursts in the IBIS/ISGRI data was carried out off-line, by examination of mask-tagged lightcurves of SGR 1935+2154 on timescales of 10, 100 ms, and 1 s, extracted using the `ii_light` program. This resulted in the discovery of seven other bursts using the 100 ms timescale (see Table 2) that were missed by the IBAS software due to their large off-axis angles.

We performed a spectral analysis for the bursts with more than 100 counts (bursts C, D, F, and I; their lightcurves are shown in Figure 3). In all cases a power-law model gave an acceptable fit and the data could not constrain the parameters of more complex models. We then computed the weighted average of their photon indexes, finding $\bar{\Gamma} = 3.2 \pm 0.5$ and imposed a Gaussian prior with these values to the photon index in the fits of the other bursts. We give all the results in Table 2,

¹⁶ It is possible to extract a spectrum in such a short time interval with the INTEGRAL Offline Scientific Analysis only starting from version 11. However, for a source with such a bright burst, we had to disable the automatic noisy pixel detection, by setting the parameter `NoisyDetFlag=0` in the program `ibis_science_analysis`.

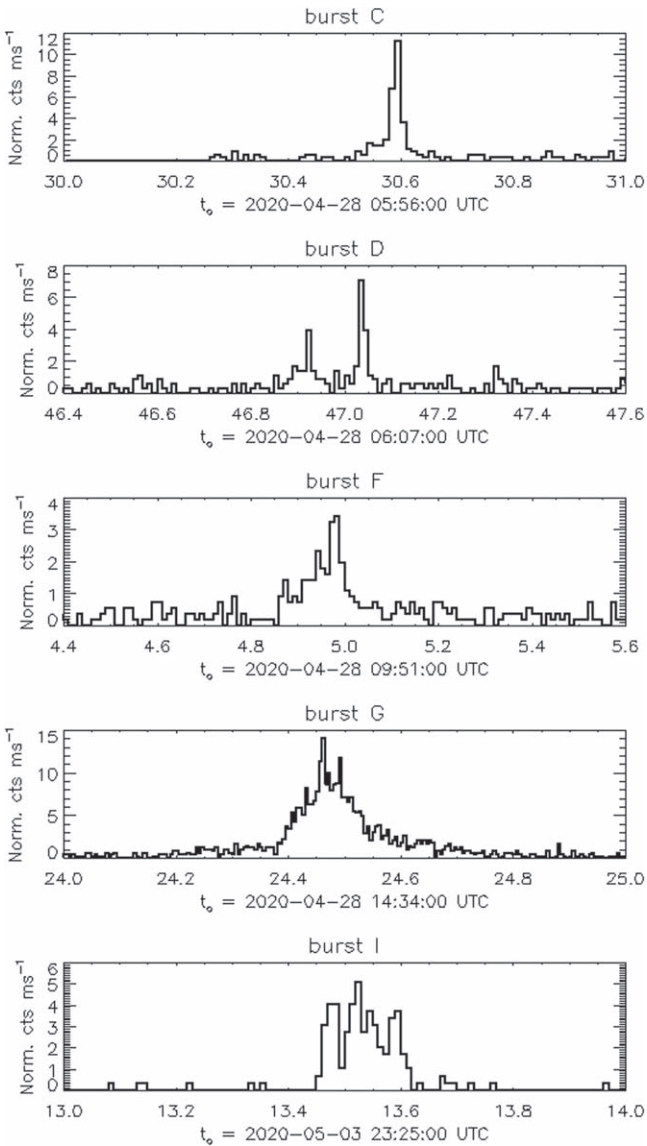


Figure 3. Lightcurves in the 20–200 keV range for the bursts of Table 2 with more than 100 counts. Time bins are of 10 ms, except for burst-G, which is binned at 5 ms. The count rates have been normalized to the values that would have been obtained with the source on-axis.

where, for the sake of comparison, the parameters of burst-G also refer to the power-law fit. All the bursts detected with high signal-to-noise ratio have spectra softer than that of burst-G.

A highly polarized burst from SGR 1935+2154 was detected by the Five-hundred-meter Aperture Spherical Telescope (FAST) on 2020 April 30 at 21:43:00.5 UTC (Zhang et al. 2020). At this time, SGR 1935+2154 was in the field of view of IBIS at an off-axis angle of $12^\circ.9$, and we could derive a 5σ upper limit on the fluence of any burst shorter than 1 s at the level of $2.3 \times 10^{-8} \text{ erg cm}^{-2}$ in the 20–200 keV band, assuming the spectral shape of burst-G. This corresponds to a ratio of radio to X-ray fluence at least six orders of magnitude smaller than that of burst-G.

3.3. Persistent Emission

No persistent hard X-ray emission from SGR 1935+2154 was detected by IBIS/ISGRI. We show in Figure 4 the upper

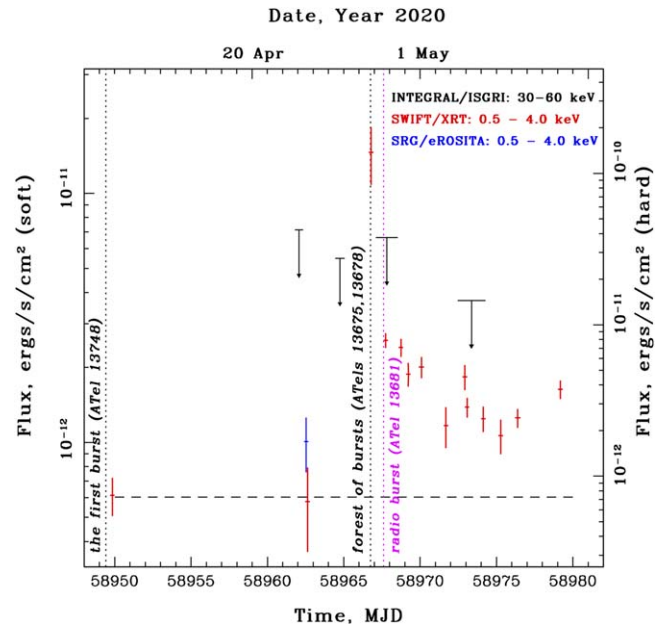


Figure 4. Evolution of the SGR 1935+2154 mean flux measured in soft X-rays with Swift/XRT (red points) and SRG/eROSITA (blue point) and upper limits from INTEGRAL in hard X-rays (black points). The horizontal dashed line shows the persistent flux level in the 0.5–4 keV energy band, calculated with parameters from Younes et al. (2017). See the text for details.

limits derived on its 30–60 keV flux from the four longest INTEGRAL observations (the first three and the last one of Table 1). To trace the overall behavior of the source, we show in the same figure its lightcurve obtained from publicly available data of the Swift/X-ray Telescope (XRT) telescope, covering the period from 2020 April 10 to May 10, and the Spectrum-Roentgen-Gamma (SRG)/eROSITA observations performed during the all sky survey on 2020 April 23 (Medvedev et al. 2020). The lightcurve in the 0.5–4 keV energy band demonstrates that the soft X-rays from SGR 1935+2154 significantly increased more than 20 times in less than 4 days before the start of the bursting activity and began to subside practically immediately after its end (see also Borghese et al. 2020).

The expected source flux in hard X-rays can be estimated using the spectral parameters obtained with the Nuclear Spectroscopic Telescope Array (NuSTAR) in the 3–79 keV energy range (Younes et al. 2017). Assuming that the spectral shape does not evolve with the flux and renormalizing the spectra with the measured fluxes in the soft energy band, we found that all IBIS/ISGRI upper limits are above the expected hard X-rays fluxes. They are also consistent with the source flux of $4 \times 10^{-12} \text{ erg cm}^{-2} \text{ s}^{-1}$ derived from the NuSTAR observation performed on May 2 (Borghese et al. 2020).

4. Distance Estimate from the Dust-scattering Ring

A bright X-ray ring, with a radius of $\sim 85''$, was detected around SGR 1935+2154 in a Swift/XRT observation performed on 2020 April 27 from 19:42 to 20:15 (Kennea et al. 2020). Its very rapid evolution (see Figure 5) excludes the possibility of a spatially extended structure at any plausible distance for SGR 1935+2154 (e.g., a magnetar wind nebula) and resembles that of rings produced by scattering of X-rays on interstellar dust grains, as seen around some GRBs and after

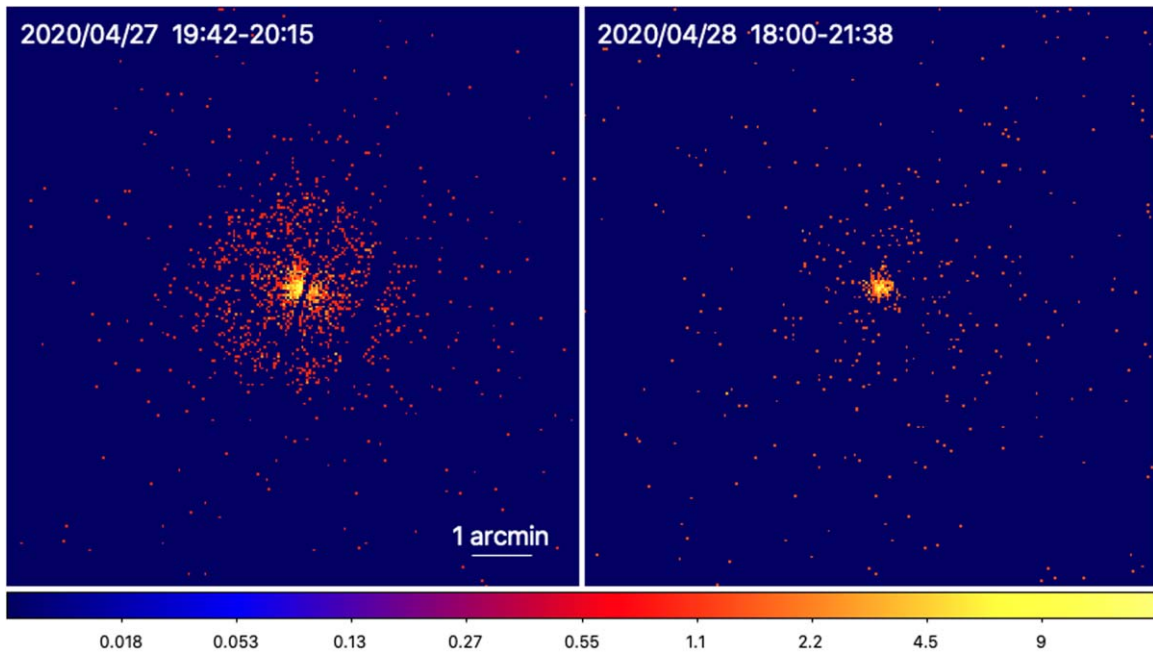


Figure 5. X-ray images (0.2–10 keV) of SGR 1935+2154 obtained with Swift/XRT on 2020 April 27 (ID 00968211001, left panel) and April 28 (ID 00033349045, right panel). The first observation clearly shows a ring of scattered emission that extends for more than $1'$ from the source. The ring was no more visible the following day, owing to its fading X-ray flux and increasing angular radius.

extremely bright magnetar bursts (see, e.g., Tiengo et al. 2010). Expanding scattering rings produced by bursting sources give the possibility of deriving some information on the distances of the emitting source and of the scattering dust by studying the time delay of scattered photons (Trümper & Schönfelder 1973).

We extracted from the XRT data (obs.ID 00968211001) three time-resolved radial profiles in the 1–5 keV energy band by dividing the observation into 11 minute intervals. The profiles were well fit with the sum of a Lorentzian, a King, and a constant function to model the ring, the SGR 1935+2154 unscattered emission, and the background, respectively. The centers of the Lorentzian curves found in the three time intervals, $79''.4 \pm 1''.9$, $85''.2 \pm 2''.5$, and $93''.2 \pm 4''.4$, clearly indicate that the ring significantly expanded during this short observation.

Due to the time delay of scattered photons, the angular radius θ of a ring produced by a burst emitted at t_B by an X-ray source at distance d_s and scattered by dust at distance d_d , increases with time t as

$$\theta(t) = \left[\frac{827}{d_s} \frac{(1-x)}{x} (t - t_B) \right]^{1/2}, \quad (1)$$

where the distances are measured in parsecs, θ in arcseconds, times in seconds, and $x = \frac{d_d}{d_s}$.

Fitting the ring expansion with Equation (1), we found t_B in the 68% c.l. interval from 18:00 to 18:50 of 2020 April 27. The main bursting activity of SGR 1935+2154 started on 2020 April 27 at 18:26:20 (Palmer 2020), but the largest X-ray fluence was produced about 5 minutes later, in a series of bright bursts emitted within ~ 10 s (Ursi et al. 2020). No other bursting episodes with similar fluence were detected in the preceding and following hours (Tavani et al. 2020b). It is therefore reasonable to attribute the origin of the X-ray ring to this “burst forest,” and fix t_B at 18:33:10.

Based on Equation (1), using the method of Tiengo & Mereghetti (2006), we assigned a pseudo-distance $D_i = 827(t_i - t_B)\theta^{-2}$ to each event i detected by XRT. The distribution of D_i values shows a clear peak centered at $D = 580 \pm 10$ pc. For an extragalactic source scattered by Galactic dust ($d_s \gg d_d$), as, e.g., in Tiengo & Mereghetti (2006) and Pintore et al. (2017), D would be a very good approximation of the dust layer distance producing the X-ray ring, whereas in the general case $D = d_d/(1-x)$.

The distribution of interstellar dust toward SGR 1935+2154 is well characterized in the 3D extinction maps of Green et al. (2019), based on Pan-STARRS 1 and 2MASS photometry and on Gaia parallaxes. These maps show that most of the optical extinction is caused by a narrow dust layer at ~ 0.5 kpc, while the rest is due to dust concentrations at ~ 1.1 and ~ 6.5 kpc. The D value derived above gives a hard upper limit on d_d , implying that only the closest dust layer can be responsible for the X-ray ring. To derive d_d more accurately, we used the Python package *dustmaps* (Green 2018) to extract the differential extinction in the SGR 1935+2154 direction from 400 to 1000 pc, with a 5 pc step, by taking the median of the five samples available in the Green et al. (2019) map, weighted on their standard deviations. The resulting extinction distribution can be well fit by a single Gaussian peak centered at 512 pc, with a standard deviation of 16 pc.¹⁷ Using this value for the dust distance, we obtain a distance of $d_s = 4.4^{+2.8}_{-1.3}$ kpc for SGR 1935+2154, independent of, but consistent with, its association with the supernova remnant G57.2+0.8.

¹⁷ To validate this method for measuring d_d , we applied the same procedure to the line of sight of GRB 160623A, where six dust-scattering rings were detected with XMM-Newton (Pintore et al. 2017). We obtain a good fit of the extinction differential distribution in the 400–1000 pc interval using the sum of three Gaussians centered at 519, 660, and 786 pc, and with standard deviations of 11, 36, and 3 pc, respectively. These distances are in very good agreement with those of the three closest dust layers derived independently (the GRB can be considered at infinite distance) from the analysis of the dust-scattering rings: 528.1 ± 1.2 , 679.2 ± 1.9 , and 789.0 ± 2.8 pc.

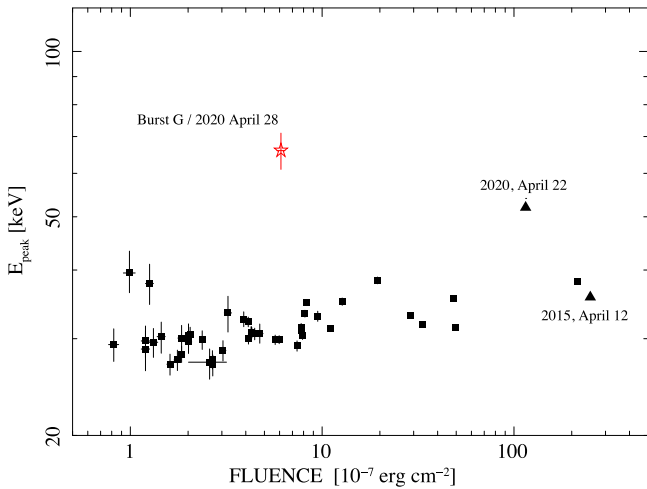


Figure 6. Peak energy vs. fluence for burst-G (red star) and other bursts from SGR 1935+2154 (squares from Lin et al. 2020a; triangles from Kozlova et al. 2016 and Ridnaia et al. 2020a).

5. Discussion

Burst-G is the first burst from an SGR to be unambiguously associated with a short pulse of radio emission with some properties similar to those of FRBs (Bochenek et al. 2020; The CHIME/FRB Collaboration et al. 2020b). It is, therefore, interesting to investigate if its high-energy properties differ from those of the bursts commonly emitted by this and other magnetars.

The 20–200 keV fluence of $(6.1 \pm 0.3) \times 10^{-7}$ erg cm $^{-2}$ and peak flux of $\sim 6 \times 10^{-6}$ erg s $^{-1}$ cm $^{-2}$, derived from the IBIS/ISGRI spectrum with the cutoff power-law model, are in the range of values previously observed for other bursts of SGR 1935+2154 (Lin et al. 2020a). Therefore, they do not qualify burst-G as particularly energetic. They correspond to a peak luminosity of $\sim 10^{40} d_{4.4}^2$ erg s $^{-1}$ and to a released energy of $\sim 1.4 \times 10^{39} d_{4.4}^2$ erg in the 20–200 keV range (assuming isotropic emission).

On the other hand, as suggested by the comparison with the other bursts in Table 2, the spectrum of burst-G was harder than those of typical SGR bursts. This can be seen, for example, by comparing its peak energy $E_p = 65 \pm 5$ keV, with the values derived by Lin et al. (2020a) for a large sample of bursts from SGR 1935+2154 observed with the Fermi/Gamma-ray Burst Monitor (GBM) instrument (see Figure 6). The distribution of E_p found by these authors is well fitted by a Gaussian centered at 30.4 keV and with $\sigma = 2.5$ keV. A similar conclusion is obtained if we compare the results of the two blackbody fits, for which we obtained temperatures a factor ~ 2.5 larger than the average values of $kT_1 = 4.4$ keV and $kT_2 = 11.3$ keV found by Lin et al. (2020a). From the spectral point of view, the SGR 1935+2154 burst most similar to burst-G was the one detected by several satellites on 2020 April 22 (Cherry et al. 2020; Hurley et al. 2020). It had a peak energy of $E_p = 52 \pm 2$ keV and a 20–200 keV fluence of $\sim 10^{-5}$ erg cm $^{-2}$ (Figure 6), but a simple time profile consisting of a single pulse lasting 0.6 s with fast rise and no evidence for substructures (Ridnaia et al. 2020a). Notably, the spectrum of burst-G was also harder than that of the intermediate flare emitted by SGR 1935+2154 on 2015 April 12. This was at least a factor 10 more energetic (Figure 6), but had $E_p = 36$ keV and a smooth time profile (Kozlova et al. 2016).

It is thus possible that the radio emission, detected so far only in burst-G, might be related to its particularly hard X-ray spectrum. Ridnaia et al. (2020b) noted that another distinctive property of burst-G might be its spiky and slowly rising lightcurve. The small number of counts of the other bursts we detected does not allow us to draw robust conclusions on this interesting possibility (Figure 3).

The triple-peaked time profile of burst-G shown in Figure 1 is particularly interesting because the time intervals between the X-ray peaks (28_{-4}^{+2} and 31_{-3}^{+2} ms) are consistent with the 29 ms separation of the two radio pulses seen by CHIME (The CHIME/FRB Collaboration et al. 2020b). The narrower component of peak 2 is centered 6.5 ± 1.0 ms after the second CHIME pulse (that is at the same time of the STARE2 pulse; Bochenek et al. 2020), but its broader component starts at a time consistent with that of the radio pulse. A similar delay, but with a larger uncertainty, is found between peak 1 and the first CHIME pulse. A physical association of the radio pulses with peaks 2 and 3 would instead imply a delay of ~ 35 ms between the X-ray and radio emission. Note that the accuracy in the relative time alignment of the radio and X-ray lightcurves is limited by the small number of X-ray counts and not by the absolute time error of the INTEGRAL data that is smaller than 0.1 ms (Kuiper et al. 2003).

The close time coincidence of the radio and X-ray emission is consistent with an origin of both components in a relatively small region of the pulsar magnetosphere (e.g., Lyutikov 2002; Wadiasingh & Timokhin 2019; Lyubarsky 2020). On the other hand, models also involving emission at distances much larger than the light cylinder radius ($Pc/2\pi = 1.5 \times 10^{10}$ cm for SGR 1935+2154) can produce (nearly) simultaneous pulses due to relativistic Doppler effects (e.g., Beloborodov 2020; Margalit et al. 2020a, 2020b).

Explanations involving magnetars at extragalactic or cosmological distances have been among the first ones to be proposed for FRBs (Popov & Postnov 2007). Several models have been developed, based on scenarios for which high-energy emission can be expected in the form of prompt bursts (e.g., Lyubarsky 2014, 2020; Beloborodov 2017, 2020) or as a long-lasting afterglow following the FRB (Murase et al. 2017). However, all the searches for X/ γ -ray counterparts of FRBs carried out up to now have been unsuccessful¹⁸ (Scholz et al. 2017; Xi et al. 2017; Cunningham et al. 2019; Guidorzi et al. 2019, 2020; Martone et al. 2019; Sun et al. 2019; Anumarlapudi et al. 2020).

Tendulkar et al. (2016) derived lower limits on the ratio between radio (1.4 GHz) and X/ γ -ray (>30 keV) fluences $\eta_{\text{FRB}} > 10^{7-9}$ Jy ms erg $^{-1}$ cm 2 for 15 FRBs. Negative results were found also with coordinated multiwavelength observations of FRB 180916.J0158+65 (Pilia et al. 2020; Scholz et al. 2020; Tavani et al. 2020b), which has been considered as a promising target, owing to its close distance of 150 Mpc and periodic behavior of the radio burst emission (The CHIME/FRB Collaboration et al. 2020a). Similarly, searches for FRBs associated with magnetar bursts provided only upper limits (Burgay et al. 2018), including the case of the 2004 December giant flare from SGR 1806–20, for which Tendulkar et al. (2016) derived $\eta_{\text{FRB}} < 10^7$ Jy ms erg $^{-1}$ cm 2 .

¹⁸ The claimed association of a ~ 400 s long X-ray transient with FRB 131104 (DeLaunay et al. 2016) has not been supported by subsequent observations (Shannon & Ravi 2017). In any case, the properties of this transient are very different from those of burst-G.

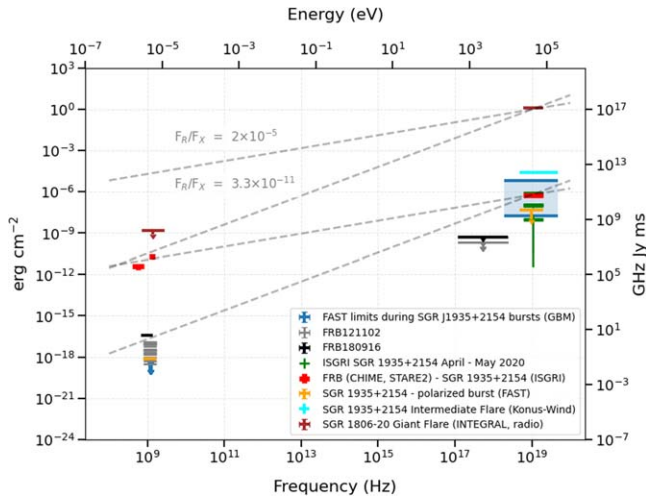


Figure 7. Comparison of the spectral energy distribution of burst-G from SGR 1935+2154 (red) with the upper limits for other magnetars and FRBs obtained from simultaneous radio and X-ray observations (Hurley et al. 2005; Kozlova et al. 2016; Tendulkar et al. 2016; Scholz et al. 2017, 2020; Bochenek et al. 2020; Lin et al. 2020b; Pilia et al. 2020; The CHIME/FRB Collaboration et al. 2020b).

Based on the radio fluences of 700 kJy ms at 600 MHz (The CHIME/FRB Collaboration et al. 2020b) and 1.5 MJy ms at 1.4 GHz (Bochenek et al. 2020), we compare the spectral energy distribution of burst-G (Figure 7) and the ratio of its radio and X-ray fluences F_R/F_X (Figure 8) with the limits obtained for other relevant events.

Burst-G was characterized by a very large value of $F_R/F_X \sim 2 \times 10^{-5}$. This high ratio is consistent with the lack of detection of high-energy emission in extragalactic FRBs, as can be seen by scaling the fluences to distances of a few hundreds of megaparsecs. On the other hand, such a high F_R/F_X is at variance with the limit derived for the SGR 1806–20 giant flare. This suggests that giant flares and ordinary SGR bursts are indeed different phenomena, as is also supported by their different spectral and timing properties, and/or that magnetar bursts can have a large range of F_R/F_X , as shown by the radio upper limits reported by The CHIME/FRB Collaboration et al. (2020b) and Lin et al. (2020b). It must also be considered that both the radio and high-energy emissions could be non-isotropic and beamed in different directions, thus complicating the observational picture and making it difficult to draw strong conclusions until a much larger sample of bursts is observed.

6. Conclusions

INTEGRAL has discovered a peculiar hard X-ray burst, characterized by the simultaneous emission of a very bright millisecond radio pulse (Bochenek et al. 2020; The CHIME/FRB Collaboration et al. 2020b), from the Galactic magnetar SGR 1935+2154. This burst was not particularly energetic at high energies, but it differed from the typical SGR bursts because of its harder spectrum. The discovery of simultaneous fast bursting emission at radio and high-energy from this Galactic source supports models based on magnetars for extragalactic FRBs, although the latter involve a larger radio energy output compared to the case discussed here.

With an analysis of the dust-scattering X-ray ring observed with Swift/XRT about one hour after a period of particularly intense bursting emission, we derived a distance of $4.4_{-1.3}^{+2.8}$ kpc

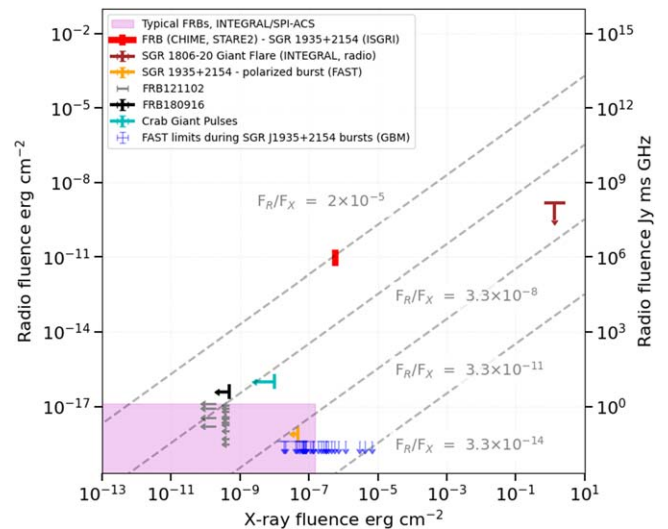


Figure 8. Radio vs. X-ray (starting from 0.5 keV) fluences for FRBs and magnetar bursts. The range of FRB fluences corresponds to a variety of detections reported in the past years (references in Figure 7 and Karuppusamy et al. 2010). The purple region indicates a robust upper limit on the hard X-ray fluence of FRBs as derived with a high-duty-cycle detector, such as the INTEGRAL SPI/ACS (Savchenko et al. 2017).

for SGR 1935+2154. We note that this value, contrary to other distance estimates, does not depend on the association of the magnetar with the supernova remnant G57.2+0.8.




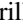


If all extragalactic FRBs were characterized by ratios of radio to X-ray fluences as large as that of burst-G from SGR 1935+2154, their detection with current high-energy satellites would be difficult. However, since it is clear that a single fluence ratio is not compatible with all available measurements (see Figure 8), future multiwavelength (and especially high-duty-cycle) observations will reveal how unusual was the, so far unique, joint detection obtained for SGR 1935+2154 and possibly confirm if, as is suggested by the INTEGRAL data, radio emission is associated only with the spectrally hardest SGR bursts or it is a more common property.

Finally, we would like to make a comment on the role of magnetars in the context of both gamma-ray bursts (GRBs) and FRBs. In the first years following their discovery, GRBs and SGRs were believed to belong to the same phenomenological class of short-lived high-energy transients of mysterious origin. However, SGRs distinguishing features of repetitive behavior, giant flares, pulsations, and association with supernova remnants along the galactic plane, convincingly demonstrated they belonged to a different population, that of galactic magnetars. On the other hand, GRBs were confirmed as cosmological sources, putting to rest one of the biggest controversies in astrophysics of the previous few decades. Newly born magnetars can also be considered as possible central engines for powering extragalactic GRBs, while a small fraction of the short-duration GRBs may be due to extragalactic magnetar giant flares.

Mirroring this GRB–SGR–magnetar entanglement, the observation of FRB-like radio emission and gamma-ray flares from the known galactic magnetar SGR 1935+2154 now opens the possibility that some of the sources that have been classified as FRBs consist of galactic magnetars so far unidentified at other wavelengths, while also providing strong support for a magnetar origin of extragalactic FRBs.

Based on observations with INTEGRAL, an ESA project with instruments and science data center funded by ESA member states (especially the PI countries: Denmark, France, Germany, Italy, Switzerland, Spain) and with the participation of Russia and the USA. ISGRI has been realized and maintained in flight by CEA-Saclay/Irfu with the support of CNES. The Italian authors acknowledge support via ASI/INAF Agreement No. 2019-35-HH and PRIN-MIUR 2017 UnIAM (Unifying Isolated and Accreting Magnetars, PI: S. Mereghetti). D.G. acknowledges the financial support of the UnivEarthS LabEx (ANR-10-LABX-0023 and ANR-18-IDEX-0001). A.L. and S.M. acknowledge the financial support of the Russian Foundation of Basic Research (proj. 19-29-11029). L.H. acknowledges support from Science Foundation Ireland grant 09/RF/AST2400. We are grateful to the Swift/XRT team for making observations open for the broad community. L.N. acknowledges support from EU Horizon 2020 Programme under the AHEAD2020 project (grant agreement No. 871158).

ORCID iDs

S. Mereghetti  <https://orcid.org/0000-0003-3259-7801>
 V. Savchenko  <https://orcid.org/0000-0001-6353-0808>
 C. Ferrigno  <https://orcid.org/0000-0003-1429-1059>
 D. Götz  <https://orcid.org/0000-0001-9494-0981>
 M. Rigoselli  <https://orcid.org/0000-0001-6641-5450>
 A. Tiengo  <https://orcid.org/0000-0002-6038-1090>
 A. Bazzano  <https://orcid.org/0000-0002-2017-4396>
 E. Bozzo  <https://orcid.org/0000-0002-7504-7423>
 A. Coleiro  <https://orcid.org/0000-0003-0860-440X>
 T. J.-L. Courvoisier  <https://orcid.org/0000-0003-2396-6249>
 M. Doyle  <https://orcid.org/0000-0001-8538-4864>
 A. Goldwurm  <https://orcid.org/0000-0003-0029-6529>
 L. Hanlon  <https://orcid.org/0000-0003-2931-3732>
 E. Jourdain  <https://orcid.org/0000-0001-9932-3288>
 A. von Kienlin  <https://orcid.org/0000-0002-0221-5916>
 A. Lutovinov  <https://orcid.org/0000-0002-6255-9972>
 A. Martín-Carrillo  <https://orcid.org/0000-0001-5108-0627>
 S. Molkov  <https://orcid.org/0000-0002-5983-5788>
 L. Natalucci  <https://orcid.org/0000-0002-6601-9543>
 F. Onori  <https://orcid.org/0000-0001-6286-1744>
 F. Panessa  <https://orcid.org/0000-0003-0543-3617>
 J. Rodi  <https://orcid.org/0000-0003-2126-5908>
 J. Rodriguez  <https://orcid.org/0000-0002-4151-4468>
 P. Ubertini  <https://orcid.org/0000-0003-0601-0261>

References

- Anumrapudi, A., Bhalariao, V., Tendulkar, S. P., & Balasubramanian, A. 2020, *ApJ*, **888**, 40
- Beloborodov, A. M. 2017, *ApJL*, **843**, L26
- Beloborodov, A. M. 2020, *ApJ*, **896**, 142
- Bochenek, C. D., Ravi, V., Belov, K. V., et al. 2020, arXiv:2005.10828
- Borghese, A., Coti Zelati, F., Rea, N., et al. 2020, arXiv:2006.00215
- Burgay, M., Esposito, P., Israel, G. L., et al. 2018, in IAU Symp. 337, Pulsar Astrophysics the Next Fifty Years, ed. P. Weltevrede et al. (Cambridge: Cambridge Univ. Press), 319
- Burgay, M., Israel, G. L., Rea, N., et al. 2014, *ATel*, **6371**, 1
- Cherry, M. L., Yoshida, A., Sakamoto, T., et al. 2020, *GCN*, **27623**, 1
- Connaughton, V., Burns, E., Goldstein, A., et al. 2016, *ApJL*, **826**, L6
- Cordes, J. M., & Chatterjee, S. 2019, *ARA&A*, **57**, 417
- Courvoisier, T. J. L., Walter, R., Beckmann, V., et al. 2003, *A&A*, **411**, L53
- Cunningham, V., Cenko, S. B., Burns, E., et al. 2019, *ApJ*, **879**, 40
- DeLaunay, J. J., Fox, D. B., Murase, K., et al. 2016, *ApJL*, **832**, L1
- Fletcher, C. & Fermi GBM Team 2020, *GCN*, **27659**, 1
- Goldwurm, A., David, P., Foschini, L., et al. 2003, *A&A*, **411**, L223
- Goodman, J., & Weare, J. 2010, *Commun. Appl. Math. Comput. Sci.*, **5**, 65
- Green, G. 2018, *JOSS*, **3**, 695
- Green, G. M., Schlafly, E., Zucker, C., Speagle, J. S., & Finkbeiner, D. 2019, *ApJ*, **887**, 93
- Guidorzi, C., Marongiu, M., Martone, R., et al. 2019, *ApJ*, **882**, 100
- Guidorzi, C., Marongiu, M., Martone, R., et al. 2020, *A&A*, **637**, A69
- Hurley, K., Boggs, S. E., Smith, D. M., et al. 2005, *Natur*, **434**, 1098
- Hurley, K., Mitrofanov, I. G., Golovin, D., et al. 2020, *GCN*, **27625**, 1, <https://gcn.gsfc.nasa.gov/gcn3/27625.gcn3>
- Israel, G. L., Esposito, P., Rea, N., et al. 2016, *MNRAS*, **457**, 3448
- Karuppusamy, R., Stappers, B. W., & van Straten, W. 2010, *A&A*, **515**, A36
- Kaspi, V. M., & Beloborodov, A. M. 2017, *ARA&A*, **55**, 261
- Kennea, J. A., Beardmore, A. P., Page, K. L., & Palmer, D. M. 2020, *ATel*, **13679**, 1
- Kothes, R., Sun, X., Gaensler, B., & Reich, W. 2018, *ApJ*, **852**, 54
- Kozlova, A. V., Israel, G. L., Svinikin, D. S., et al. 2016, *MNRAS*, **460**, 2008
- Kuiper, L., Hermsen, W., Walter, R., & Foschini, L. 2003, *A&A*, **411**, L31
- Labanti, C., di Cocco, G., Ferro, G., et al. 2003, *A&A*, **411**, L149
- Lebrun, F., Leray, J. P., Lavocat, P., et al. 2003, *A&A*, **411**, L141
- Levan, A., Kouveliotou, C., & Fruchter, A. 2018, *ApJ*, **854**, 161
- Li, C. K., Lin, L., Xiong, S. L., et al. 2020, arXiv:2005.11071
- Lin, L., Göğüş, E., Roberts, O. J., et al. 2020a, *ApJ*, **893**, 156
- Lin, L., Zhang, C. F., Wang, P., et al. 2020b, arXiv:2005.11479
- Lyubarsky, Y. 2014, *MNRAS*, **442**, L9
- Lyubarsky, Y. 2020, *ApJ*, **897**, 1
- Lytikov, M. 2002, *ApJL*, **580**, L65
- Marcote, B., Nimmo, K., Hessels, J. W. T., et al. 2020, *Natur*, **577**, 190
- Margalit, B., Beniamini, P., Sridhar, N., & Metzger, B. D. 2020a, arXiv:2005.05283
- Margalit, B., Metzger, B. D., & Sironi, L. 2020b, *MNRAS*, **494**, 4627
- Martone, R., Guidorzi, C., Margutti, R., et al. 2019, *A&A*, **631**, A62
- Medvedev, P. S., Sunyaev, R. A., Gilfanov, M. R., et al. 2020, *ATel*, **13723**, 1
- Mereghetti, S., Götz, D., Borkowski, J., Walter, R., & Pedersen, H. 2003, *A&A*, **411**, L291
- Mereghetti, S., Pons, J. A., & Melatos, A. 2015, *SSRv*, **191**, 315
- Murase, K., Mészáros, P., & Fox, D. B. 2017, *ApJL*, **836**, L6
- Olausen, S. A., & Kaspi, V. M. 2014, *ApJS*, **212**, 6
- Palmer, D. M. 2020, *ATel*, **13675**, 1
- Palmer, D. M., Barthelmy, S., Gehrels, N., et al. 2005, *Natur*, **434**, 1107
- Pearlman, A. B., Majid, W. A., Prince, T. A., Naudet, C. J., & Kocz, J. 2020, *ATel*, **13713**, 1
- Petroff, E., Hessels, J. W. T., & Lorimer, D. R. 2019, *A&ARv*, **27**, 4
- Pilia, M., Burgay, M., Possenti, A., et al. 2020, *ApJL*, **896**, L40
- Pintore, F., Tiengo, A., Mereghetti, S., et al. 2017, *MNRAS*, **472**, 1465
- Platts, E., Weltman, A., Walters, A., et al. 2019, *PhR*, **821**, 1
- Popov, S. B., & Postnov, K. A. 2007, arXiv:0710.2006
- Prochaska, J. X., Macquart, J.-P., McQuinn, M., et al. 2019, *Sci*, **366**, 231
- Ranasinghe, S., Leahy, D. A., & Tian, W. 2018, *OphJ*, **4**, 1
- Ravi, V., Catha, M., D'Addario, L., et al. 2019, *Natur*, **572**, 352
- Ridnaia, A., Golenetskii, S., Aptekar, R., et al. 2020a, *GCN*, **27631**, 1
- Ridnaia, A., Svinikin, D., Frederiks, D., et al. 2020b, arXiv:2005.11178
- Savchenko, V., Bazzano, A., Bozzo, E., et al. 2017, *A&A*, **603**, A46
- Scholz, P., Bogdanov, S., Hessels, J. W. T., et al. 2017, *ApJ*, **846**, 80
- Scholz, P., Cook, A., Cruces, M., et al. 2020, arXiv:2004.06082
- Shannon, R. M., & Ravi, V. 2017, *ApJL*, **837**, L22
- Stamatikos, M., Malesani, D., Page, K. L., & Sakamoto, T. 2014, *GCN*, **16520**, 1
- Sun, S., Yu, W., Yu, Y., Mao, D., & Lin, J. 2019, *ApJ*, **885**, 55
- Surnis, M. P., Krishnakumar, M. A., Maan, Y., Joshi, B. C., & Manoharan, P. K. 2014, *ATel*, **6376**, 1
- Tavani, M., Casentini, C., Ursi, A., et al. 2020a, arXiv:2005.12164
- Tavani, M., Verrecchia, F., Casentini, C., et al. 2020b, *ApJL*, **893**, L42
- Tendulkar, S. P., Kaspi, V. M., & Patel, C. 2016, *ApJ*, **827**, 59
- The CHIME/FRB Collaboration, Amiri, M., Andersen, B. C., et al. 2020a, arXiv:2001.10275
- The CHIME/FRB Collaboration, Andersen, B. C., et al. 2020b, arXiv:2005.10324
- Tiengo, A., & Mereghetti, S. 2006, *A&A*, **449**, 203
- Tiengo, A., Vianello, G., Esposito, P., et al. 2010, *ApJ*, **710**, 227
- Trümper, J., & Schönfelder, V. 1973, *A&A*, **25**, 445
- Turolla, R., Zane, S., & Watts, A. L. 2015, *RPPH*, **78**, 116901
- Ubertini, P., Lebrun, F., di Cocco, G., et al. 2003, *A&A*, **411**, L131
- Ursi, A., Pittori, C., Tempesta, P., et al. 2020, *ATel*, **13682**, 1

Vedrenne, G., Roques, J. P., Schönfelder, V., et al. 2003, *A&A*, 411, L63
Veres, P., Bissaldi, E., Briggs, M. S. & Fermi GBM Team 2020, GCN, 27531, 1
von Kienlin, A., Beckmann, V., Rau, A., et al. 2003, *A&A*, 411, L299
Wadiasingh, Z., & Timokhin, A. 2019, *ApJ*, 879, 4

Xi, S.-Q., Tam, P.-H. T., Peng, F.-K., & Wang, X.-Y. 2017, *ApJL*, 842, L8
Younes, G., Guver, T., Enoto, T., et al. 2020, *ATel*, 13678, 1
Younes, G., Kouveliotou, C., Jaodand, A., et al. 2017, *ApJ*, 847, 85
Zhang, C. F., Jiang, J. C., Men, Y. P., et al. 2020, *ATel*, 13699, 1
Zhou, P., Zhou, X., Chen, Y., et al. 2020, arXiv:2005.03517